

Rapid and sensitive detection of cancer-derived small extracellular vesicles using Janus particles

Received: 24 June 2024

Accepted: 10 February 2026

Published online: 11 March 2026

 Check for updatesSonu Kumar^{1,3}, John Alex Sinclair^{1,3}, Tiger Shi¹, Han-Sheng Chuang^{1,2}, Satyajyoti Senapati¹ & Hsueh-Chia Chang¹ ✉

Detecting small extracellular vesicles is critical for understanding disease biology and developing diagnostic tools, yet current methods require lengthy isolation steps and lack sensitivity owing to interference from abundant proteins. Here we report on an assay that uses Janus particles that enable rapid, isolation-free detection by exploiting Brownian rotation-induced blinking changes. When vesicles bind, their size significantly alters the blinking frequency, while smaller proteins produce no signal, ensuring selectivity. Using less than 10 μl of sample, the assay detects approximately 200 vesicles per microlitre and works directly on plasma, serum, urine and cell media in under 1 h. In a blind study of 87 subjects with colorectal cancer, pancreatic ductal adenocarcinoma, glioblastoma, Alzheimer's disease and healthy controls, the method identified disease type with an area under the curve of 0.90–0.99. Compared with ultracentrifugation combined with surface plasmon resonance, which requires 24 h, our approach delivers 2 orders of magnitude better sensitivity and dynamic range, offering a fast and robust platform for clinical and research applications.

Small extracellular vesicles (sEVs) are lipid-bilayer-enclosed particles containing important cargo, including protein and nucleic acids, depending on their nature of biogenesis and cellular origin^{1–6}. Secreted by cells into the extracellular matrix, they often contribute to cell-to-cell paracrine communication over a short distance^{7–12}. However, many find their way into human plasma, potentially offering avenues for surveying the cellular landscape with a simple blood draw^{13–17}. The extracellular matrix can especially become leaky for cancer and several other diseases to escalate sEV escape and disease dissemination far from the primary site^{18,19}. This amplified release of sEVs into the microcirculation from diseased cells further enhances its prognosis and diagnosis potential^{20–23}. In addition, the unique surface markers on sEVs, which facilitate their uptake by specific cells—including the exchange between cancerous and healthy cells—present a novel strategy for targeted therapy^{24–28}. By leveraging these markers, therapies can be designed

to selectively deliver drugs directly to cancer cells, minimizing harm to healthy tissue. Therefore, profiling surface markers on sEVs presents valuable opportunities across diagnostics, therapeutics and drug delivery, underscoring its extensive potential in advancing medical science.

Quantifying surface markers on sEVs suffers from several challenges and limitations—these sEV surface markers can also appear in non-vesicular forms, such as soluble entities^{29,30}. Often, only the vesicular proteins are enzymatically active or have higher activity and hence are the relevant markers^{31–36}. Furthermore, these surface markers can be present alongside non-sEV proteins such as albumin, which exists in concentrations over a billion-fold higher than sEVs in biofluids²⁹ such as human plasma—non-specific adsorption of these non-sEV proteins can interfere with any immunoassay^{37,38}. Thus, traditional methods frequently necessitate an sEV isolation step to eliminate surface markers in non-vesicular forms and non-sEV-associated contaminating proteins

¹Department of Chemical and Biomolecular Engineering, University of Notre Dame, Notre Dame, IN, USA. ²Department of Biomedical Engineering, National Cheng Kung University, Tainan, Taiwan. ³These authors contributed equally: Sonu Kumar, John Alex Sinclair. ✉e-mail: hchang@nd.edu

found in unprocessed biofluids^{29,30,39}. Ultracentrifugation is the most common isolation step before any sample characterization. With its high capital cost and bulky instruments, this cumbersome and tedious process tremendously hampers parallelization and field application. Moreover, the yield of sEV isolation cannot be consistent every time, thus introducing a yield bias owing to isolation alone.

Even after isolating sEVs, other challenges complicate the characterization methods to permit the sub-picomolar detection limit necessary for sEV quantification. For example, after isolation, sEVs often aggregate⁴⁰, thus requiring immediate characterization, while the isolation step creates lipoprotein aggregates that are difficult to distinguish from sEVs⁴¹. Given that sEVs are sized between proteins and cells, many techniques originally designed for proteins and cells—such as western blot and flow cytometry, respectively—have been adapted for sEVs^{41–46} without fully addressing their unique challenges. Techniques such as western blot heavily depend on contamination-free samples, which are challenging to obtain even after extensive isolation steps^{47–50}. Larger sEVs with higher cargo capacities can mask the cargo of the diagnostically relevant smaller sEVs, making protein-based sEV assays suffer from bias and reduced sensitivity. Meanwhile, flow cytometry struggles to detect particles below cellular dimensions; even state-of-the-art nano-flow cytometry faces difficulties identifying particles smaller than 100 nm owing to their low time of flight⁵¹, often requiring extensive labelling and a low limit of detection^{51–54}. Other recently proposed methods include interferometry-based ExoView, which has only one log dynamic range, preventing it from studying less abundant sEV fractions and requiring extensive pretreatment and labelling^{55,56}. Other proposed methods in literature have reasonable sensitivity but require extensive labelling or pretreatment for sEVs^{57,58}. A gold standard for sEV characterization, with standardized isolation and pretreatment procedures, is hence still unavailable.

Therefore, an enrichment-free, sensitive and rapid characterization method is needed for sEVs in biofluids, such as plasma, serum, urine and even cell culture media, to be practical for clinical applications. Herein we present the immunojanus particles (IJPs) that can profile sEVs without enrichment and are less prone to direct matrix interference. These IJPs are micrometre-sized spherical particles with one fluorescent half and one non-fluorescent half. The fundamental basis of detection relies on the rotational Brownian motion that these particles undergo; a blinking effect similar to stars blinking in the night sky results from the thermal kicks that alternatively expose the fluorescent or non-fluorescent sides. The frequency of this blinking is highly sensitive, and the binding of any biological particle >50 nm can significantly affect its blinking rate, which is ideal for sEV detection. Abundant proteins such as albumin and soluble versions of the targeted marker on sEVs are too small to produce any signal, allowing us to selectively quantify sEVs from plasma, serum, urine and cell media using less than 10 μ l of sample volume with a limit of detection of \sim 200 sEV μ l⁻¹. In addition, because these beads are suspended in a solution, the long incubation period associated with mass transfer-limited surface assays is shortened significantly as sEVs only need to diffuse to the nearest bead. Mass transfer limitation (faster kinetics than diffusion rate) ensures that the signal follows a universal scaling with all antibodies that satisfy the mass transfer limitation. This eliminates the variation that comes with the different affinity of antibodies from various sources, but also different affinities of the same antibody with a heterogeneous population of antibodies owing to steric hindrance or avidity in a small subfraction of the sEVs, which means that capture fraction is not representative of the bulk. Utilizing this unique feature, the IJP platform can circumvent issues often accompanied by varying antibody affinities and sources.

Using our IJP platform, we can screen and identify different diseases (in a blind setting) using sEV surface markers in a mixed pool of 87 human subjects with colorectal cancer, pancreatic ductal

adenocarcinoma, glioblastoma, Alzheimer's disease and healthy subjects. We achieved high sensitivity and specificity without needing sample pretreatment and directly from human plasma in under 60 min. We have thoroughly benchmarked our platform against a day-long ultracentrifugation (UC) and surface plasmon resonance (SPR), which produced results consistent with IJPs but with reduced sensitivity and selectivity.

Results

The IJP platform

We synthesized IJPs by creating a monolayer of fluorescent polystyrene particles on a glass slide. Following this, a gold layer approximately 10 nm thick was deposited onto the upper surface, giving the particles a Janus configuration with two distinct faces. Figure 1a provides a schematic depiction of the IJPs, illustrating micrometre-sized spheres with one hemisphere being fluorescent and the other coated with gold. This configuration produces a blinking fluorescence effect when observed under a microscope, as the non-fluorescent gold and fluorescent polystyrene alternate owing to Brownian rotation.

The gold hemisphere is functionalized with target-specific antibodies to capture relevant biological entities within a sample. Figure 1b shows multiple Janus particles under a fluorescence microscope, and Fig. 1c illustrates their blinking behaviour, typically about 1 s. Scanning electron microscope (SEM) analysis in Fig. 1d reveals the topography and composition of the two hemispheres, highlighting their contrasting characteristics. Energy dispersive X-ray spectroscopy (EDX) imaging confirmed the presence of a gold-like element on one hemisphere and a carbonaceous element similar to polystyrene on the other, demonstrating the Janus nature.

After functionalizing the gold hemisphere with antibodies, we allowed the IJPs to bind to antigens on sEVs that are specific to these antibodies. However, other nanocarriers such as lipoproteins or soluble versions of these proteins can also bind to the antibodies on the IJP surface. In addition, many non-specific proteins may bind non-specifically to the surface owing to van der Waals forces, ionic interactions and hydrophobic forces. This poses a significant challenge because our objective is to characterize sEVs without any isolation steps, such as UC, which typically removes these soluble and non-specific proteins. In the following sections, we will discuss the specificity of the signal and how our platform addresses these challenges. An important observation is that binding sufficiently large biological entities such as sEVs to the IJPs significantly reduces the blinking frequency. This change is attributed to the increased drag exerted by the biological particle as it rotates within the surrounding fluid. Figure 1e illustrates the mechanism used for the IJP signal, involving simple mixing and incubation procedures.

To accurately characterize sEVs, it is essential to determine the blinking periods of hundreds of IJPs per frame over extended durations. This requires the automated detection and tracking of IJPs within a frame, followed by calculating the average blinking frequency. For detection and tracking purposes, our focus is primarily on the change in intensity of the IJP fluorescence rather than high-definition imaging that reveals particle topology. High-resolution imaging typically depends on image segmentation and mask-based methods that utilize discontinuity detection or greyscale similarity and require expensive instrumentation for capturing high-resolution images. Moreover, incorporating more Janus particles per frame at lower magnification, instead of capturing high-resolution images of fewer IJPs at higher magnification, enhances our statistical analysis. This approach provides a more robust distribution of blinking periods by looking at the rate of change of particle intensity, leveraging the increased IJP sample size to improve the accuracy and reliability of our measurements while also requiring cheaper fluorescent optical systems. We report the change in blinking as the change in ensemble average of blinking rate across all IJPs.

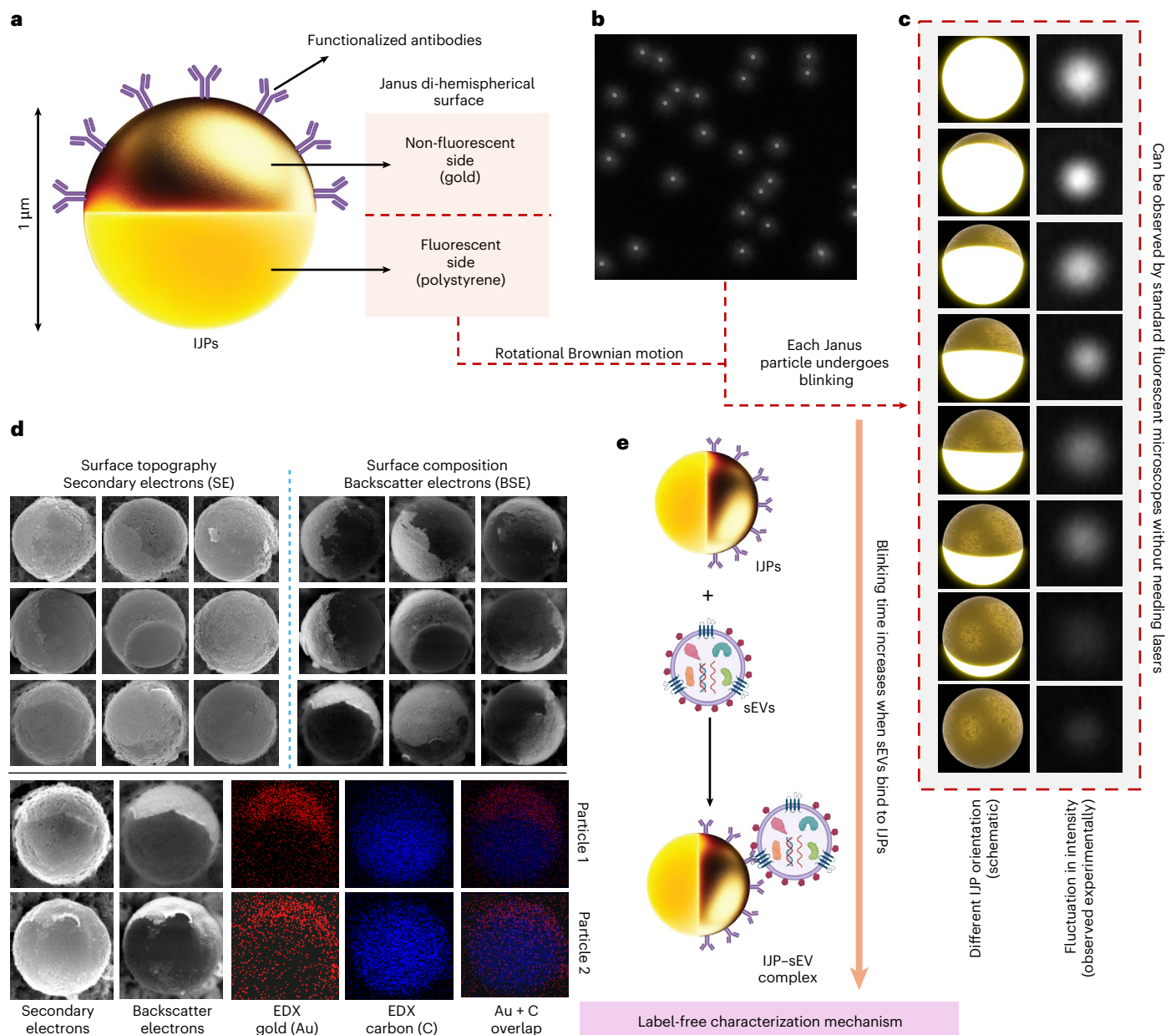


Fig. 1 | IJPs are di-hemispherical micrometre-sized particles with one fluorescent side that makes them blink. a, The schematic shows IJPs with an immunogold surface on one half (non-fluorescent) and a fluorescent half on the other, allowing the particle to switch between fluorescent and non-fluorescent states depending on orientation. **b**, A snapshot captures dozens of IJPs in solution, each undergoing individual blinking. **c**, Owing to rotational Brownian motion, different sides of the particles are oriented at different times, altering the intensity and causing the blinking effect. The left panel of **c** illustrates how different orientations result in high or low intensity, observed experimentally

in the right panel. **d**, SEM images reveal the spherical surface topography of IJPs using secondary electrons. Surface composition analysis using backscatter electrons shows one half of the particles covered with gold, consistent with the EDX detector findings, indicating gold (or a similar atomic number element) deposition on one half, making them appear brighter with backscatter electrons. **e**, Schematic representation of the IJP-sEV complex and its relative increase in the time period compared with a blank IJP particle. Figure created in BioRender; Kumar, S. <https://BioRender.com/p9infwc> (2025).

We use a distinct methodology for detecting IJPs and processing low-resolution images/videos, which involves multiplying the image by a dilation matrix corresponding to the feature size of JPs in these images to enlarge any high intensity point with a similar feature size. Post-dilation, we utilize a disk detection method based on accumulation points referred to as the circular Hough transform⁵⁹⁻⁶¹ to detect the IJPs in the image, as shown in Fig. 2a. The detected centres are then mapped back onto the original image and tracked across subsequent frames. Key metrics, such as the intensity of the particle, are analysed using wavelet techniques to determine the frequency of blinking.

Larger aggregates, which do not blink owing to their non-Janus nature and large size, are excluded by thresholding and focusing on the range of frequencies typical for Janus particles. This algorithm and its applications are detailed in Fig. 2a, and all the intensities are measured by looking within the proximity of the detected centre of the IJPs in the raw unprocessed footage.

Characterization of sEVs using IJPs

To characterize sEVs, we used a straightforward method that involves mixing IJPs with sample solutions and observing their blinking

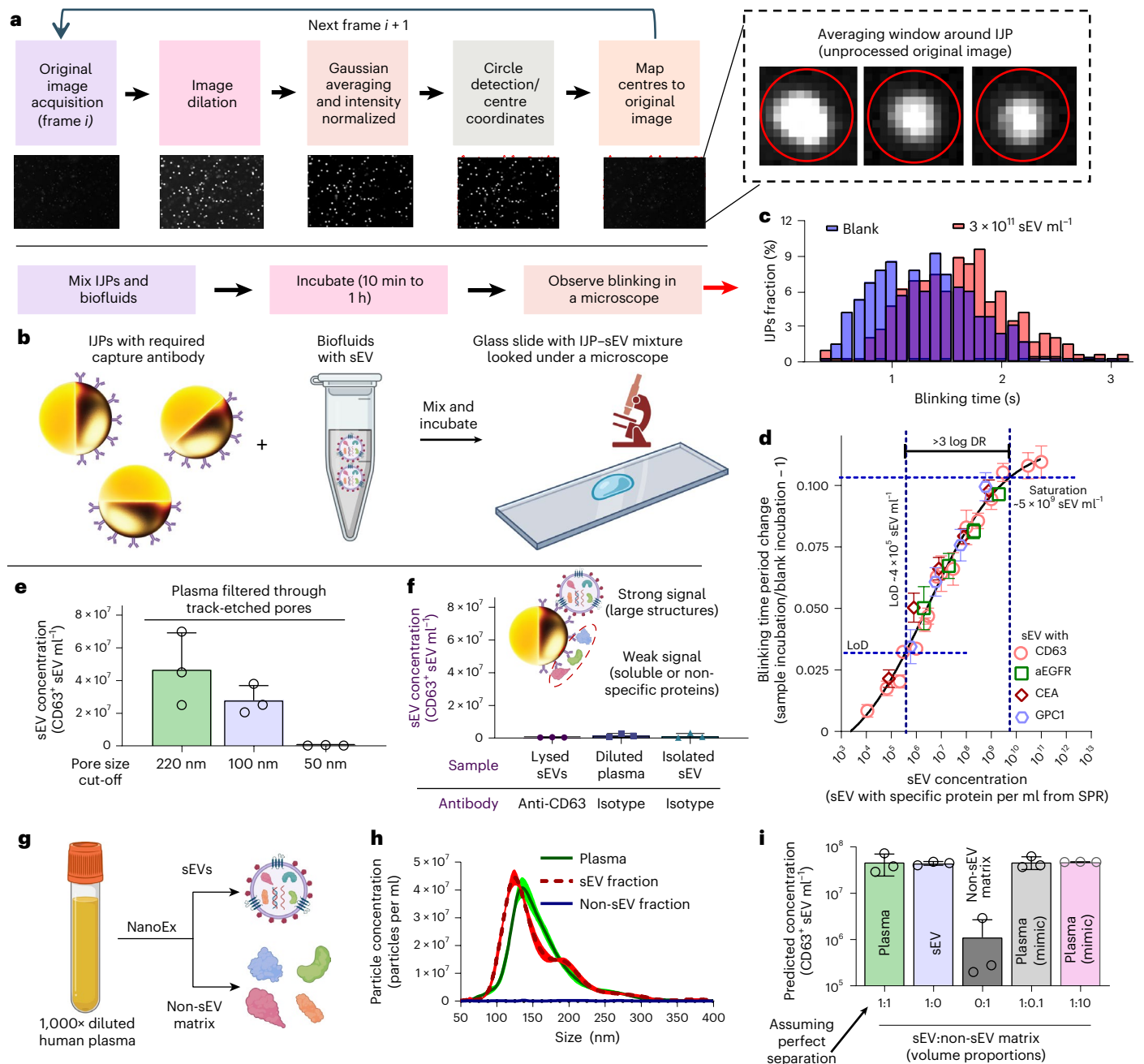


Fig. 2 | Characterization of sEVs using IJPs. **a**, An automated algorithm for tracking individual IJPs, which involves image acquisition, dilation, Gaussian averaging, intensity normalization, circle detection and mapping centres to the original image. **b**, The experimental process where IJPs with required capture antibodies are mixed with biofluids containing sEVs, incubated for 10 min to 1 h and observed under a microscope for blinking. **c**, Histogram plot shows the shift in the blinking time period of particles upon mixing with sEVs ($3 \times 10^{11} \text{ ml}^{-1}$) compared with blank (PBS). **d**, Scatter plot provides a calibration curve for IJPs coated with anti-CD63, anti-aEGFR (mab806), anti-CEA and anti-GPC1 against sEV concentration derived from SPR for isolated sEVs from DiFi cell line ($n = 2$) and human plasma samples ($n = 3$). Error bars represent standard error. **e**, Bar plot shows signal variation from plasma filtered through 220 nm, 100 nm and 50 nm filters, indicating IJPs' immunity to signals from species below 50 nm.

Most sEVs are 50–200 nm, thus 100 nm filtering reducing the signal, while 50 nm suppresses it. Error bars represent one standard deviation. **f**, Bar plot highlights that lysed sEVs (detergent-treated) with anti-CD63 capture, diluted plasma with isotype capture and isolated sEV with isotype capture produce no signal. **g**, The process of splitting plasma into sEV and non-sEV matrix fractions to create mimic plasma by mixing varying proportions of the two fractions. **h**, Line plot presents NTA data for the split sEV and non-sEV fractions. **i**, Bar plot compares the signal produced by plasma, isolated sEV, non-sEV matrix, plasma (mimic) with a tenth of the non-sEV matrix, and plasma with ten times the non-sEV matrix. Error bars represent one standard deviation. For panels with error bars (**d–f, h, i**), one biological replicate is used to demonstrate analytical performance but statistics are not derived from it. Figure created in BioRender; Kumar, S. <https://BioRender.com/ySg9trc> (2025).

behaviour under a fluorescence microscope, as illustrated in Fig. 2b. One significant advantage of using micrometre-sized IJPs is their ability to settle under gravity at a modest but noticeable rate. This settling allows the IJPs to move out of the microscope's focal plane after

measurements, continuously replaced by particles from the liquid above in the droplet. This process eliminates the need for microscopes equipped with z-stacking capabilities or microfluidic devices to supply fresh IJPs in-frame for measurements. Furthermore, this method

Table 1 | IJP platform assay parameters

Metric	Method	Result
LoB	Concentration at ~ mean of blank + $1.65 \times \sigma$ (blank)	5×10^4 sEV ml ⁻¹
LLOD	LoB + $1.65 \times \sigma$ (blank)	4×10^5 sEV ml ⁻¹
LLOQ	Lowest point in calibration curve where CV < 20%	1×10^6 sEV ml ⁻¹
Intra-day precision	Same sEV aliquot measured on same IJP batches	CV = 16%
Lot-to-lot precision	Different sEV aliquot (same biological replicate) measured on different IJP batches	CV = 27%
Back-interpolated accuracy	Measuring known standards and measuring accuracy as % of original concentration measured	97% (3×10^6 sEV ml ⁻¹) 87% (3×10^7 sEV ml ⁻¹) 101% (2×10^8 sEV ml ⁻¹)
EV spike recovery	Final concentration of 5×10^7 sEV ml ⁻¹ spike in $10 \times$ diluted plasma matrix (sEV depleted) in $1,000 \times$ diluted plasma matrix (sEV depleted)	104% 104%

All parameters are calculated for >200 blinking IJPs per replicate. Numbers can be different if averaged over fewer IJPs and if the sEVs aggregate during storage. These parameters can also be reduced by averaging over more IJPs.

facilitates extended observation periods, enhancing the statistical reliability of our measurements as more IJPs are analysed. Typically, imaging across a 60–120 s duration proves sufficient for gathering statistically representative data. In addition, given that the micrometre-sized IJPs generally exhibit a blinking period of 1–2 s, a standard camera with a frame rate of 10–30 frames per second can effectively capture this blinking. Therefore, the equipment required for IJP experiments is already available in most biological research laboratories. This ubiquity allows for the seamless integration of IJP methodologies into existing lab set-ups, enhancing their accessibility and facilitating adoption without requiring specialized equipment. It should be noted that the reported blinking periods represent the ensemble average across all IJPs.

Figure 2c shows the significant shift in blinking periods of IJPs with anti-CD63 capture when incubated with phosphate-buffered saline (PBS) (blank) compared with isolated 3×10^{11} sEV ml⁻¹ derived from human plasma. This shift can be calibrated against known concentrations of isolated sEVs, as shown in Fig. 2d for different capture antibodies on IJPs, showing a lower limit of detection (LLOD) of 4×10^5 sEV ml⁻¹ (limit of blank (LoB) = 5×10^4 sEV ml⁻¹) and >3 log₁₀ dynamic range. The lower limit of quantification (LLOQ) is 1×10^6 sEV ml⁻¹, and the assay remains linear from 1×10^6 sEV ml⁻¹ to 1×10^9 sEV ml⁻¹ on a semi-log concentration–signal plot. Repeatability, intra-/inter-day variation (intra-day coefficient of variation (CV%) = 16%) and lot-to-lot precision (CV = 27%) are within the accepted range for sEV assays, and back-interpolated accuracy across 3 standard levels spans 87–101%. In simulated plasma experiments, spike-in recovery is 104% in both 10- and 1,000-fold diluted, sEV-depleted matrices. Full validation data, including precision metrics, accuracy and recovery, are provided in Table 1. Calculation was done using independently drawn calibration curve using anti-CD63⁺ IJPs. We have also shown robustness in the blinking time period distribution in Supplementary Fig. 1.

It is important to note that all antibodies for various proteins fall on the same universal curve for the IJPs when calibrated against the actual concentration of sEVs with that specific protein using SPR. This occurs because we ensure a high probe concentration on the IJP surface with high-affinity antibodies, meaning that the reaction between sEV and capture antibody on the IJP is very fast (proportional to the product of surface coverage and the on-rate of antibodies); thus, they are limited

by the diffusion of sEV from the bulk to the IJPs, which provides the universal scaling and hence removes any antibody-to-antibody variation. Furthermore, this approach significantly reduces biases that might arise owing to steric hindrance or avidity effects, particularly with sEVs that may have proteins adjacent to the target protein, exhibit slightly different conformations with exposed epitopes or have a high density of surface proteins facilitating multivalent binding. These factors typically influence the kinetic on-rate and off-rate but are effectively neutralized under conditions where diffusion-limited mass transfer predominates, ensuring that the captured sEV fractions are truly representative of the bulk. This is discussed more in subsequent sections with further proofs.

We know that sEVs typically range from 50 nm to 200 nm in size, and therefore, using track-etched pores with no tortuosity allows us to filter out entities larger than the pore size from the biofluid. We applied this method to filter human plasma in three different ways and analysed flow-through samples: the first strategy is with a 220 nm pore, which should not remove any sEVs; the second strategy is with a 100 nm pore, which should remove a significant number of sEVs larger than 100 nm but not all; and the third strategy is with a 50 nm pore, which removes all sEVs. As shown in Fig. 2e, no significant signal is observed for the 50 nm filter, while the 100 nm filter shows a reduced signal compared with the 220 nm filter. This indicates that our platform is exclusively sensitive to larger structures, and entities smaller than 50 nm do not produce a signal. This is crucial as it selects against lipoproteins in plasma, a significant source of false signals in sEV assays, which are typically smaller than 50 nm. This unique size-dependent characteristic of our IJP assay platform enables the use of a simple pre-filtration step, in which the plasma samples are passed through a 220 nm porous membrane to remove any entities or interfering protein aggregates bigger than 220 nm, resulting in relatively cleaner samples for the assay.

Moreover, protein aggregates can potentially be a significant source of signal on the IJP surface. Figure 2f shows that using an isotype control under identical functionalization parameters produced no signal, effectively ruling out protein aggregates interacting with the IJP surface. In addition, the treatment of sEVs with non-denaturing detergent, which does not lyse protein aggregates, resulted in no signal, as shown in Fig. 2f. This indicates that lysed sEVs release all their proteins into an almost soluble form owing to the detergent disrupting the lipid bilayer. Yet these soluble protein counterparts, despite binding to IJPs, do not produce any significant change in blinking signal. This is essential information because when IJPs are incubated in plasma, they encounter numerous proteins associated with sEVs. However, these same proteins could potentially be presented in a soluble form or on other lipoproteins. Therefore, the fact that entities smaller than 50 nm, which include both soluble proteins and lipoproteins, cannot produce a signal thus confirms that IJPs can effectively address these challenges and potentially quantify sEVs directly from plasma.

To further demonstrate that the non-sEV component of plasma does not generate a signal, we utilized a recently commercialized NanoEx by Aopia Biosciences. This device efficiently separates plasma into sEV-containing and non-sEV matrices, as illustrated in Fig. 2g, with a non-tortuous asymmetric membrane (Fig. 2h). This separation enables us to isolate plasma and create simulated plasma by adjusting the sEV to non-sEV ratio through recombination. In Fig. 2i, we show that simulated plasma with 10% or 1,000% of the original non-sEV matrix/sEV ratio performs similarly to the plasma while maintaining the 3 samples maintained the same sEV concentration (see Methods for preparing simulated plasma). This finding indicates that the soluble fraction in plasma has a negligible effect on the signal, thereby making IJPs highly resistant to interference. It should be noted that signals may still be produced when an antibody cross-reacts to other proteins on sEVs, such as the LICAM false-positive previously reported for sEVs⁶². Nevertheless, it falls within the scope of immunology to identify more specific antibodies, as non-specific antibodies can generate signals

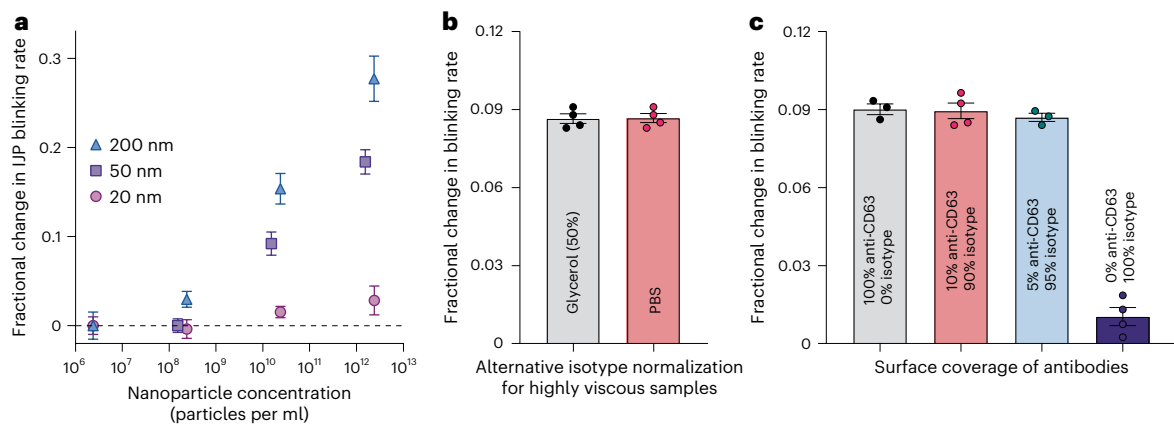


Fig. 3 | Illustrating the effect of particle size and surface marker coverage on the blinking rate of IJPs, highlighting the transport-limited nature of binding. **a**, The change in blinking rate with anti-biotin-conjugated IJPs incubated with nanoparticles of different sizes. The calibration plot is slightly shifted from that for sEVs owing to the highly negative zeta potential of these nanoparticles compared with the less negative sEVs trying to bind to the highly negative gold surface. **b**, Alternative normalization for highly viscous samples: typically, normalization uses IJPs with an antibody to the surface marker incubated with a blank, but this approach uses isotype controls directly

with the sample. **c**, Competitive crosslinking alters antibody surface coverage, showing no correlation with surface coverage of target antibodies, suggesting transport-limited binding independent of on-rate, off-rate or antibody concentration. This is evident from overlapping calibration plots with different antibodies using IJP against the true sEV concentration with that specific marker. Data are presented as mean \pm standard deviation from single validated lot of the nanoparticles. Error bars are used to represent the variation among technical replicates.

even in sandwich assays. The only known platform capable of handling such non-specific reactions is the proximity ligation assay, which faces its own challenges and requires extensive pretreatment owing to using interference-prone polymerase chain reaction (PCR) to generate signals. However, a significant advantage of our platform is that if an antibody non-specifically reacts with a protein not present on sEVs, it does not generate any signal. This is a notable improvement over platforms such as western blot or SPR, where signals are still produced when non-specific proteins are captured, whereas IJPs do not generate signals for entities smaller than 50 nm even if antibodies cross-react with non-sEV fraction.

Universal normalization of blinking signal to enhance reproducibility

In our study, we conducted a series of experiments using biotinylated nanoparticles of varying sizes to evaluate the performance of IJPs conjugated with anti-biotin antibodies to demonstrate the size dependence of blinking in a more controlled setting. Specifically, we utilized biotinylated beads of 20 nm, 50 nm and 200 nm to represent different particle populations within our samples (Fig. 3a). The choice of anti-biotin over streptavidin for surface functionalization was deliberate as anti-biotin exhibits orders-of-magnitude lower affinity than the streptavidin–biotin pair⁶³. Replacing it with streptavidin would introduce a tetrameric protein with exceptionally high avidity. This would complicate direct comparisons with the other monoclonal antibodies evaluated in this study, unlike anti-biotin, which also serves as a monoclonal antibody. Thus, the use of anti-biotin ensured consistency with our existing experimental protocols for antibody conjugation and highlighted the high sensitivity of our system. The results demonstrated that the IJPs exhibited a strong and specific binding to the biotinylated beads, with the signal intensity correlating with the size of the nanoparticles, with negligible signal with 20 nm nanoparticles, which would generally represent lipoproteins and smaller non-specific species in a biological setting. This finding underscores the robustness of our platform in detecting sEVs and other nanoscale entities, while effectively excluding signals from smaller contaminants such as lipoproteins.

Furthermore, we investigated the effect of antibody density on the surface of IJPs, revealing that the system operates in a diffusion-limited

regime, where the observed response is largely independent of antibody affinity consistent with our universal calibration curve (Fig. 2d). This phenomenon is well documented in our previous work³² as well as in techniques such as SPR^{64,65}, where mass transfer limitations can obscure the intrinsic kinetics of binding interactions. To validate this hypothesis, we used a competition-based functionalization approach, introducing isotype antibodies as competitors to modulate the surface density of target-specific antibodies. Our results showed that varying the antibody density did not significantly affect the reaction rate, confirming that the system is dominated by diffusion rather than affinity. Only a negligible change in signal is observed, despite a 20-fold reduction in antibody concentration, thus confirming that the binding is diffusion-controlled (Fig. 3c). This is very useful as it can allow for (a) a universal calibration plot with different antibodies targeting different proteins as long as the calibration is done against the true concentration of sEVs with that specific marker, and (b) same calibration plot for antibody targeting same protein but different epitopes of it. In addition, no signal is produced with isotype, which confirms the high specificity of the signal.

Moreover, while our primary experiments demonstrated that 50 \times diluted plasma viscosity remains relatively stable and does not significantly impact the blinking rate of IJPs, we explored an alternative normalization approach to address potential viscosity-related variability in high-viscosity samples. By conducting experiments with IJPs functionalized with target antibodies and isotype control antibodies, we were able to normalize the blinking rates obtained from the isotype controls (as opposed to normal blank controls with IJPs with target antibodies), effectively removing the effects of non-specific interactions and viscosity. This method proved effective even in samples resuspended in 50% glycerol, which has roughly 10 times the viscosity of PBS (Fig. 3b). The consistency of our results across different viscosity conditions reinforces the robustness of our platform and its applicability to a wide range of biofluid samples.

Direct detection of sEVs across various biofluids using IJPs and their orthogonal comparison using UC + SPR

This section outlines the characterization of different proteins on sEVs from various sources, including cell media (DiFi, GBM9, MDA-MB-468, A375P and 3T3), human serum and urine. The method produces protein

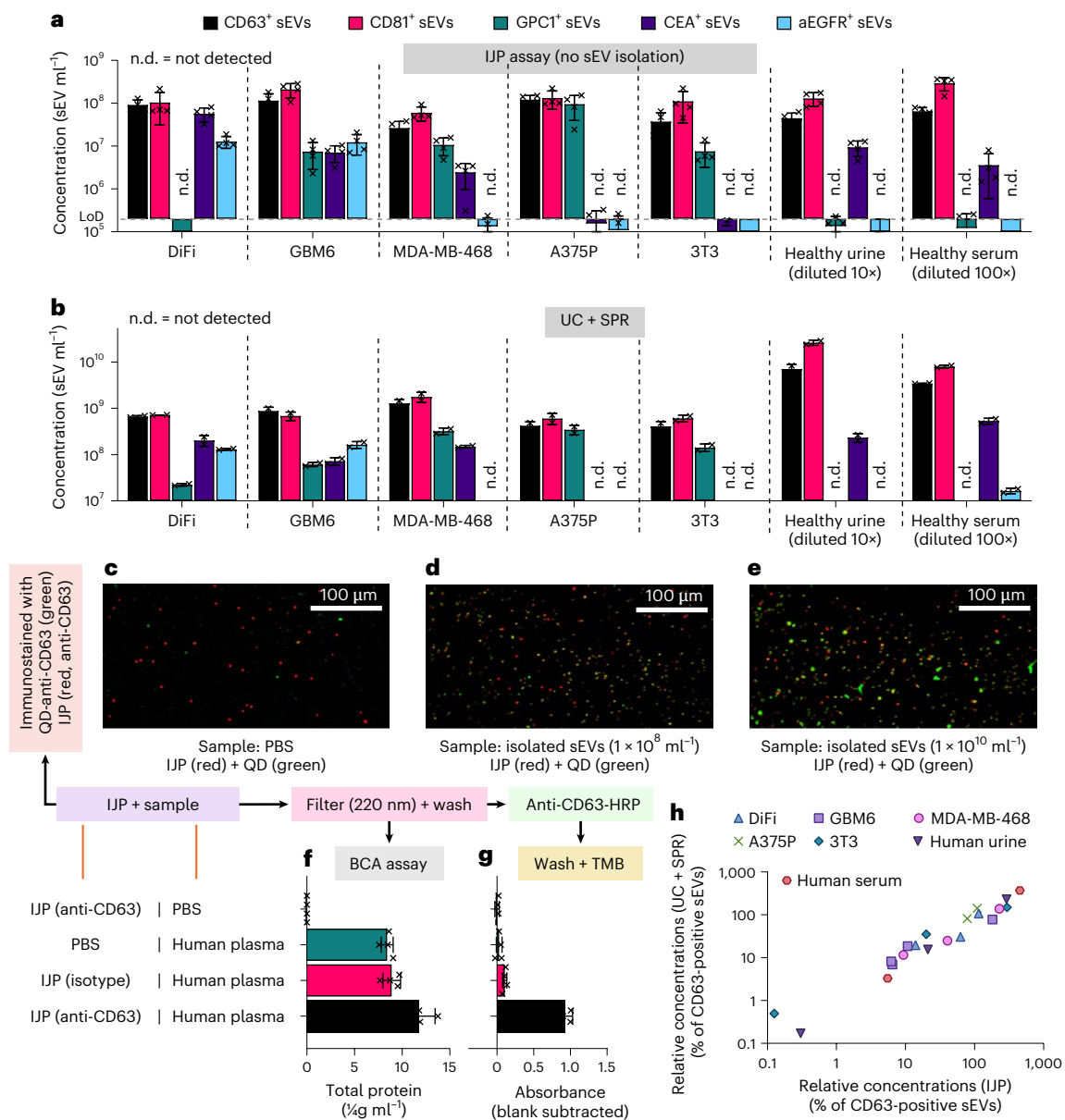


Fig. 4 | Comparing IJP characterization to orthogonal UC (isolation) + SPR (characterization) (UC + SPR) and further controls for IJPs.

a, Characterization of CD63⁺, CD81⁺, GPC1⁺, CEA⁺ and aEGFR⁺ sEVs in cell media (DiFi, GBM6, MDA-MB-468, A375P and 3T3) and human biofluids (urine and serum) using IJPs. **b**, Characterization of the same sEVs using UC + SPR, showing identical results. **c–e**, Immunostaining of IJPs (red) with anti-CD63 capture mixed with samples containing QDs labelled with anti-CD63 (green): PBS (**c**), 1 × 10⁸ sEV ml⁻¹ (**d**) and 1 × 10¹⁰ sEV ml⁻¹ (**e**). **f**, BCA assay of IJPs mixed with 10× diluted human plasma, filtered with 220 nm and washed with PBS, showing high non-specific binding of proteins for controls that do not change the blinking rate. **g**, Instead of the BCA assay, anti-CD63 with HRP is added and washed,

followed by an enzymatic reaction with 3,3',5,5'-tetramethylbenzidine (TMB). IJPs producing significant shifts in blinking are highly enriched in anti-CD63, while those that do not change blinking significantly do not produce a high signal in this assay, despite having similar total protein concentrations as shown in **f**. **h**, UC + SPR and IJPs show a linear trend for the relative expression of different sEVs normalized by CD63⁺ sEVs. Error bars represent one standard deviation. Data are presented as mean ± standard deviation from one biological replicate from different cell lines. The same replicate is used to compare IJPs to orthogonal platforms. Panels **c–e** show representative zoomed-in images at different concentrations of sEVs to demonstrate IJP–sEV binding.

concentrations comparable to those obtained through UC followed by SPR analysis, with both methods showing similar relative expressions. Measurements of CD63⁺, CD81⁺, CEA⁺, GPC1⁺ and aEGFR⁺ sEVs using IJP and UC + SPR, as shown in Fig. 4a,b, respectively, indicate identical trends and relative differential expressions. A challenge with SPR is the detection of soluble proteins even post-UC; hence, double pelleting and resuspension were performed to ensure high purity of sEVs. The consistent results between the IJP platform, which takes under 60 min, and the UC + SPR platform, which requires almost a day, across various cell culture media as well as human and

urine suggest that IJPs can effectively and rapidly characterize sEVs with minimal interference.

To verify that IJPs (red fluorescence) are capturing sEVs, we incubated anti-CD63-functionalized IJPs with PBS (control), 1 × 10⁸ sEV ml⁻¹ and 1 × 10¹⁰ sEV ml⁻¹, along with anti-CD63-conjugated quantum dots (QDs) (green fluorescence), as illustrated in Fig. 4c–e, respectively. These figures show an increase in green fluorescence correlating with sEV concentration, underscoring the lower detection limits of fluorescence-based methods. Notably, QDs, known for their high fluorescence, produce weak signals at 1 × 10⁸ sEV ml⁻¹, whereas IJPs

detect significantly lower concentrations of sEVs. Additional controls included incubating IJPs with samples, followed by mixing, filtering through a 220 nm filter and performing a PBS wash, which were then analysed for total protein and captured sEV. Specifically, total protein was measured using a bicinchoninic acid (BCA) assay (Fig. 4f) and anti-CD63 was detected using an enzymatic reaction with horseradish peroxidase (HRP)-conjugated anti-CD63 (Fig. 4g) on these captured beads. Figure 4f indicates minimal non-specific binding to the IJPs (most on the 220 nm membrane based on control with no-IJP), while Fig. 4g shows substantial anti-CD63 binding in the positive controls, demonstrating the sensitivity and specificity of these assays. Owing to the low sensitivity of the BCA and enzymatic immunoassays, a large volume of IJPs and samples was required to produce detectable signals, even with human plasma.

We analysed the data from Fig. 4a,b, which measured sEV concentrations using the IJP platform and UC + SPR, respectively. We compared these results, normalized to CD63⁺ sEVs and found that the IJP platform, without involving an isolation step, performed similarly to UC + SPR, as shown in Fig. 4h. This strong correlation indicates that IJPs can directly characterize a wide range of untreated biofluids, making the isolation step unnecessary when the characterization of sEV surface markers is the only objective.

Rapid screening of different diseases using sEVs in human plasma

In this study, we introduce one of the initial applications of disease screening using sEV surface markers, using the IJP platform within a diverse cohort of human subjects. This pilot study includes individuals diagnosed with colorectal cancer (CRC), pancreatic ductal adenocarcinoma (PDAC), glioblastoma multiforme (GBM), Alzheimer's disease (AD) and healthy controls. Our selection aims to reflect a realistic hospital setting where patients with various diseases coexist with healthy individuals, contrasting sharply with single-disease models that only incorporate one disease type alongside healthy subjects.

A primary challenge in global health is the accurate differentiation of healthy individuals from those with diseases and further pinpointing the specific disease. To address this, we selected four distinct sEV surface markers, each associated with specific diseases: conformationally active EGFR (mab806) for GBM, carcinoembryonic antigen (CEA) as a tumour marker for CRC and as a gastrointestinal tissue marker, glypican-1 (GPC1) for PDAC and phosphorylated Tau181 (pTau181) for AD. These markers were chosen for their established links to these diseases, although the overexpression of markers in diseases other than those expected remains a significant screening challenge within a multi-disease cohort.

Our findings identified distinctive profiles of sEV populations: aEGFR⁺ sEVs were significantly elevated in GBM and CRC samples, but not in healthy, AD or PDAC samples, as shown in Fig. 5a. Conversely, GPC1⁺ sEVs were elevated in GBM, CRC and PDAC (Fig. 5b), while CEA⁺ sEVs showed pronounced elevation primarily in CRC (Fig. 5c). On the basis of these observations, we developed a straightforward multi-disease screening protocol illustrated in Fig. 5d. Initially, we test for aEGFR⁺ sEVs, which stratifies our cohort into those with overexpression (GBM and CRC) and those without (healthy, PDAC and AD), achieving an area under the curve (AUC) of 0.9899 and *P* values around 2×10^{-4} (Fig. 5e,i). For patients with overexpression (CRC or GBM), subsequent testing for CEA⁺ sEVs enables differentiation between GBM (no overexpression) and CRC (overexpressed CEA⁺ sEVs), with an AUC of 0.9602 and *P* value $\sim 2 \times 10^{-4}$ (Fig. 5f,j). Conversely, if aEGFR⁺ sEVs are not overexpressed, we proceed with testing for GPC1⁺ sEVs, facilitating differentiation between PDAC (overexpressing) and healthy/AD (no overexpression), with an AUC of 0.9279 and *P* value $\sim 1 \times 10^{-2}$ (Fig. 5g,k). If GPC1⁺ sEVs show no overexpression, we then test for pTau181⁺ sEVs, which allows differentiation among healthy, AD and mildly cognitively impaired (MCI) subjects, with an AUC of 1 between healthy and AD and

a *P* value of 5×10^{-11} (Fig. 5h,l). This methodology offers a highly accurate approach for disease detection within a cohort using sEV markers characterized by IJPs.

To demonstrate the consistency of these results, we conducted orthogonal measurements of the patient samples using UC + SPR, with Fig. 6a–c (heat map showing mean expression in Fig. 6g) serving as orthogonal counterparts to Fig. 5a–c, showing a similar trend across the disease groups. Owing to yield bias between samples, we normalized all concentrations for UC + SPR against CD63⁺ sEVs, thus preventing direct comparison with IJP, which measures raw sEV concentration, whereas UC + SPR measures a normalized fraction. We also show that sEV-associated cargo is better than the total cargo found in plasma with total CEA for healthy and CRC shown in Supplementary Fig. 2.

However, plotting the different proteins between IJP and UC + SPR for the three proteins (Fig. 6d–f) also shows a similar trend, confirming that IJP is suitable for direct disease type detection with enhanced sensitivity and significantly reduced time requirement (under 60 min for IJP compared with almost a day for UC + SPR).

Discussion

Highly abundant plasma markers such as CEACAM5 are readily quantifiable only in plasma (or serum) by enzyme-linked immunosorbent assay (ELISA) (Supplementary Fig. 2); however, their signal is substantially reduced following extracellular vesicle (EV) isolation, consistent with limited association of these markers with EVs. As IJP only produces signals from proteins associated with EVs, this study introduces IJPs as an effective tool for the direct characterization of sEVs in biofluids, circumventing the need for previous isolation. Our results demonstrate that IJPs can accurately profile sEV surface markers with high sensitivity and specificity, directly from biofluid samples such as plasma, serum and urine, and are robust against interference from dispersed proteins. The ability to rapidly detect and characterize sEVs from low-volume samples not only offers a practical advantage over traditional methods but also improves the throughput and reliability of biomarker analysis in clinical settings. Unlike methods such as Nanosight, which analyse the overall population of sEVs and similarly sized nanocarriers, our platform provides high sensitivity for detecting sEVs expressing a specific surface marker. This targeted approach enables more precise and biologically relevant measurements.

In the context of state-of-the-art vesicle analytics, the IJP platform delivers performance metrics that compare favourably with, and in several dimensions exceed, leading clinical and research-grade EV assays. Conventional approaches—nanoparticle tracking analysis (NTA), ExoView, ELISA, nano-flow cytometry and SPR—typically require extensive enrichment of sEVs, depend on labelling or exhibit compromised sensitivity when confronted with high-protein biofluids^{48–50,52–54,64,65}. By contrast, our enrichment-free workflow achieves a limit of blank of $\sim 5 \times 10^4$ sEV ml⁻¹, a lower limit of detection of $\sim 4 \times 10^5$ sEV ml⁻¹ and a lower limit of quantification of $\sim 1 \times 10^6$ sEV ml⁻¹, while maintaining a >3-log dynamic range. Operational precision remains within accepted analytical bounds (intra-day CV $\sim 16\%$ and lot-to-lot CV $\sim 27\%$), and spike-in recovery in sEV-depleted plasma remains consistently high (104% in both $10\times$ and $1,000\times$ diluted matrices). These parameters outperform many isolation-dependent assays, which often exhibit markedly lower recovery, poorer linearity and higher susceptibility to non-vesicular interference biofluids^{48–50,52–54,64,65}. Notably, our assay's ability to maintain accuracy and precision across heterogeneous plasma backgrounds—combined with matrix tolerance to non-sEV fractions—positions IJPs as a next-generation vesicle characterization solution capable of meeting both clinical throughput requirements and research reproducibility standards. Moreover, the receiver operating characteristic (ROC) curves for different cohorts with IJP and UC + SPR produce similar AUC values despite much shorter time requirement (Supplementary Fig. 3).

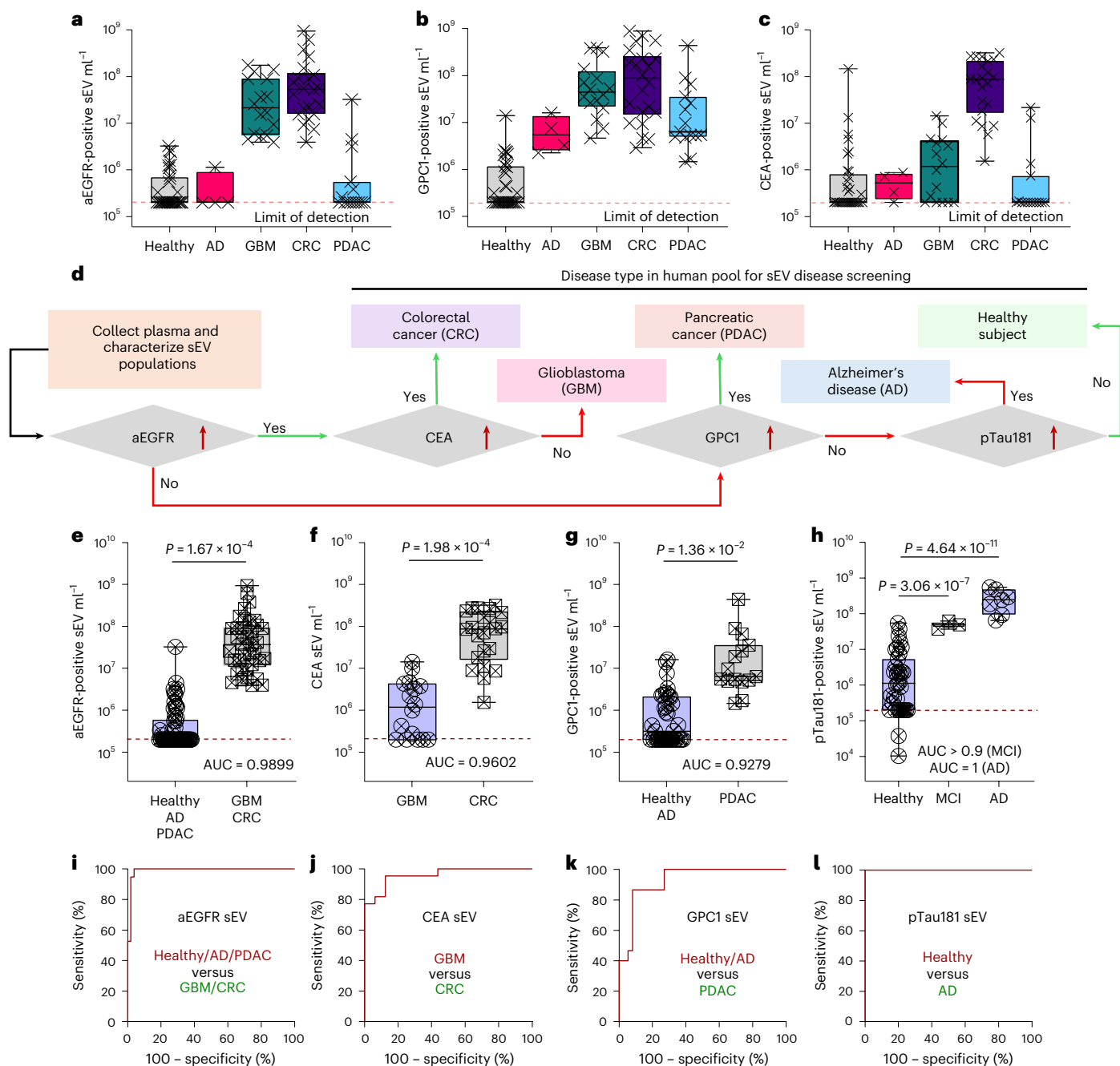


Fig. 5 | A blink disease screening 60 min protocol using IJPs with 87 human subjects comprising healthy individuals, patients with colorectal cancer (CRC), patients with pancreatic adenocarcinoma (PDAC), patients with glioblastoma (GBM) and patients with Alzheimer’s (AD), using their plasma directly. **a–c**, Typical sEV-specific protein population profiling of human plasma for aEGFR⁺ sEVs (**a**), GPC1⁺ sEVs (**b**) and CEA⁺ sEVs (**c**) using the box and whisker plot. **d**, Schematic diagram illustrating the process of disease type screening in human plasma samples for sEVs. Plasma samples are collected, and sEV populations are characterized. The presence of specific sEV populations determines further testing with specific overexpressions of aEGFR⁺, GPC1⁺ and pTau181⁺ sEVs yielding a corresponding disease. **e**, Overexpression of aEGFR⁺ sEVs occurs only in GBM and CRC, not in healthy, AD and PDAC, ruling out multiple diseases. **f**, Upon overexpression of aEGFR⁺ sEVs, testing for CEA⁺ sEV overexpression allows differentiation between subjects with GBM (underexpression) and CRC (overexpression). **g**, If aEGFR⁺ sEVs are not overexpressed, GPC1⁺ sEVs are tested, with healthy and AD showing no

overexpression but PDAC being highly overexpressed. **h**, If GPC1⁺ sEVs are not overexpressed, pTau181⁺ sEVs are checked to differentiate between healthy individuals and AD patients. **i–l**, ROC plots corresponding to the diagnostic performance of IJPs (**i–l** correspond to **e–h**, respectively in that order). Panels **e–g** are represented using box and whisker plot with central line being the median, box being the 25th and 75th quantile, and whiskers representing 0th and 100th quantile. Box plots (**a–c**): centre line, median; box bounds, 25th–75th percentiles; whiskers, minimum to maximum. Sample sizes are independent human subjects: healthy $n = 33$, AD $n = 4$, GBM $n = 16$, CRC $n = 22$ and PDAC $n = 15$. Statistical analysis (**e–h**): two-tailed unpaired *t*-test assuming equal variances, no adjustment for multiple comparisons. The human samples were collected from subjects ageing 30–80 with 50% male and 50% female for all groups. PDAC had 8 M and 7 F. The correlation with age and gender is avoided owing to low sample size. Data distribution was assumed to be normal, but this was not formally tested.

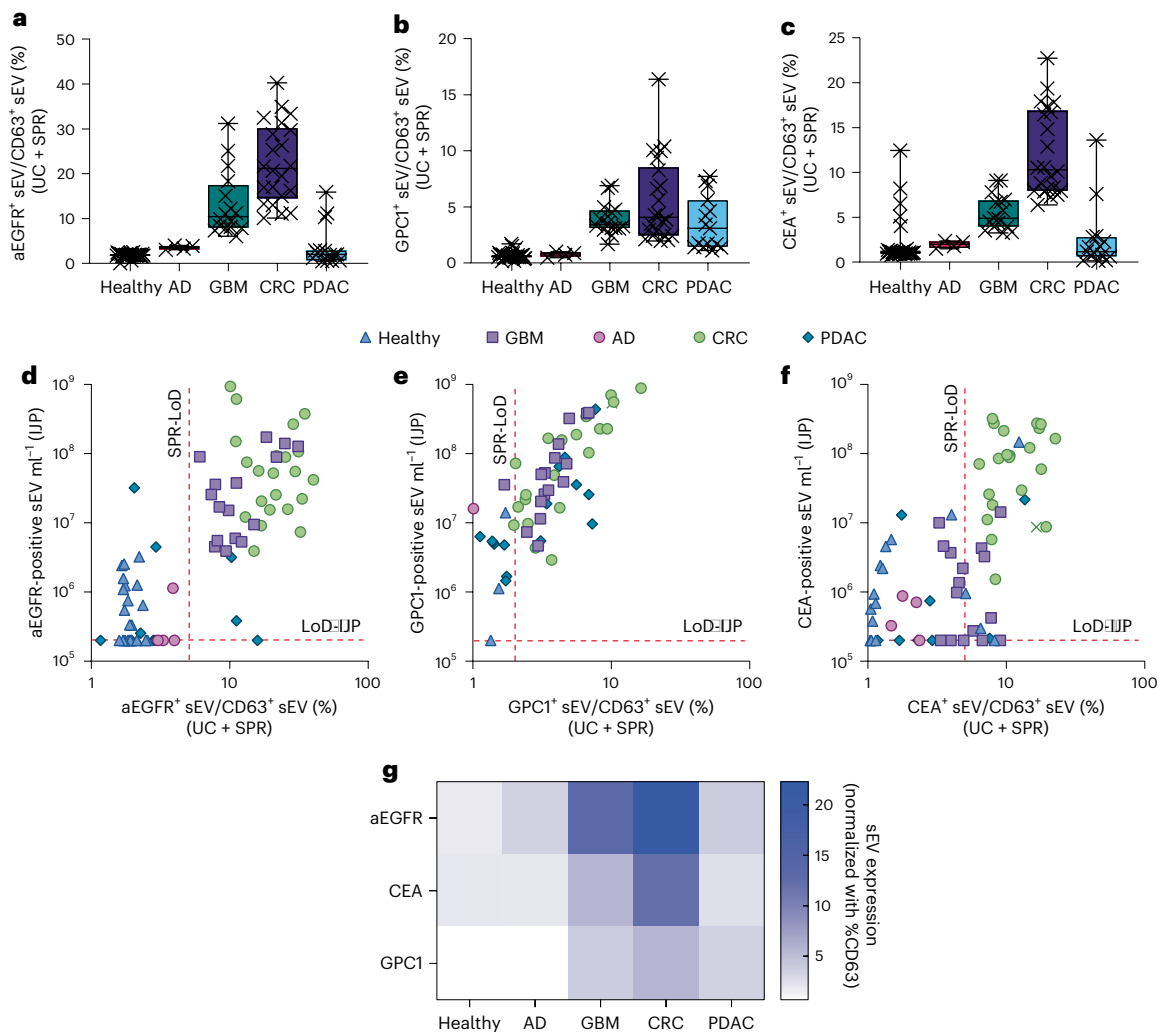


Fig. 6 | Orthogonal characterization for disease screening using sEV markers with UC + SPR. **a–c**, Box and whisker plots corresponding to the aEGFR⁺ (**a**), GPC1⁺ (**b**) and CEA⁺ (**c**) sEV populations, respectively, using UC + SPR. The results and trends are consistent with those obtained using IJPs, with UC + SPR taking over 24 h compared with less than 1 h with IJPs. The box and whisker plots have a central line being the median, box being the 25th and 75th quantile, and whiskers representing 0th and 100th quantile. **d–f**, Comparisons of the expression levels of aEGFR⁺ (**d**), GPC1⁺ (**e**) and CEA⁺ (**f**) sEVs, respectively, across the human subjects when measured using IJP versus UC + SPR (normalized by CD63⁺ sEVs). The low sensitivity (several subjects below the limit of detection in SPR) and yield bias of UC, and the complexity associated with isolating relatively pure sEVs from human plasma compared with cell media, show a rough qualitative trend

with clustering around the diagonal line with aEGFR⁺ sEVs showing moderate correlation (>0.3) and GPC1⁺ and CEA⁺ sEVs showing strong correlation (>0.5). In addition, SPR is more prone to producing false signals from soluble proteins in non-vesicular fraction compared with IJPs that does not produce any signal for particles smaller than 50 nm. **g**, Heat map showing sEV expression (normalized by CD63) from different patient cohorts. Box plots (**a–c**): centre line, median; box bounds, 25th–75th percentiles; whiskers, minimum to maximum. Sample sizes: healthy $n = 30$, AD $n = 4$, GBM $n = 16$, CRC $n = 22$ and PDAC $n = 15$ independent subjects analysed by UC + SPR. The human samples were collected from subjects ageing 30–80 with 50% male and 50% female for all groups. PDAC had 8 M and 7 F. The correlation with age and gender is avoided owing to low sample size. Data distribution was assumed to be normal, but this was not formally tested.

The application of IJPs in a pilot study involving a mixed cohort of patients with different diseases and healthy controls underscores the method's clinical relevance, particularly in the rapid screening of disease states. By providing a robust and streamlined approach to sEV analysis, IJPs hold potential for significant impacts in the fields of diagnostics and therapeutic monitoring, where quick and accurate biomarker assessment is critical. Because clinical sEV workflows, biobank standard operating procedures (SOPs) and all comparative EV-diagnostic platforms universally rely on plasma or serum rather than whole blood, our study focused on these acellular biofluids; evaluating whole blood as a potential future matrix represents an interesting extension but falls outside the scope of the present validation. Further refinement and validation of this technology could lead to its adoption in routine clinical diagnostics, offering a non-invasive means for disease detection and management and a means for accelerating sEV research.

Methods

Ethical statement

The studies involving human participants were reviewed and approved by the Indiana University Institutional Review Board (study number 1105005445) and the Institutional Ethics Committee at Austin Health. The patients/participants provided written informed consent to participate in this study. All ethical regulations relevant to human research participants were followed. We received pancreatic adenocarcinoma sample from Indiana Biobank, CRC from Precision for Medicine, Alzheimer's from Precision for Medicine and Indiana Biobank, glioblastoma from Andrew Scott and Hui Gan, Tumour Targeting Laboratory, ONJCRI and all healthy samples from Precision for Medicine. All ethical regulations relevant to human research participants were followed^{31,32,36,66–68}. Covariates associated with the samples are provided in Supplementary Table 1.

IJP fabrication

The IJPs were produced in-house using 1.0 µm FluoSpheres Polystyrene Microspheres from Thermo Fisher Scientific (catalogue number F13081/F13083). The beads were diluted to 0.1% solids in 70% (v/v) isopropyl alcohol (VWR, catalogue number BDH7999-4). A plain microscope slide (VWR, catalogue number 48300-026) was treated with plasma for 15 s using an Electro-Technic Products Model BD-20 High Frequency Generator. The dilute FluoSpheres suspension (1 ml) was deposited onto a slide and left for multiple hours—overnight to allow the isopropyl alcohol to evaporate completely. Once dried, the slide was inserted into an AIRCO Temescal FC 1800 electron beam vacuum deposition/thin-film coater system and coated with 30 nm of gold at a rate of 0.5 Å s⁻¹. The gold-coated slide was then removed and sonicated in an ultrasonic cleaner (Branson, catalogue number 5510R-DTH) for 15 min. The released particles were collected in a 1% (v/v) Tween 20 (Sigma-Aldrich P9416-50ML)/deionized (DI) H₂O solution and filtered 3 times using a 5 µm disk filter (Cytiva Whatman Puradisc, catalogue number 10463533) to remove any aggregates and other large impurities. The particle suspension was concentrated to approximately 1 × 10⁸ particles per ml and stored in a 4 °C fridge until needed^{66,68}.

We used 1 × 10⁷ IJP particles per ml for all experiments, as this particle concentration is the lowest concentration that can still provide quantitative capture and a reliable analytical signal. This rationale is based on our assumption that each 1 µm IJP carries 10⁴ antibodies, which corresponds to approximately 1 × 10¹¹ antibodies per ml or about 170 pM. The equilibrium dissociation constant of high-affinity monoclonal IgGs is in the 10–100 pM range⁶⁹. The assay is thus operating above that range, ensuring that the binding is limited by vesicle availability rather than the antibody density. Therefore, 1 × 10⁷ IJP particles per ml represents the lowest practical concentration that still provides quantitative capture. The pre-conjugated IJPs were stable at 4 °C for several months. The conjugated IJPs were used within the same day^{66,68}.

Antibody functionalization on IJP

The gold hemisphere of the Janus particles was functionalized with target-specific antibodies using the Abcam Gold Conjugation Kit (ab154873). Up to 5 µl of antibodies underwent a buffer exchange using a 10 K molecular weight cut-off (MWCO) centrifugal filter (Thermo-Fisher Scientific, catalogue number 88513) and 400 µl DI H₂O. Antibodies were diluted to 0.1 mg ml⁻¹ using the provided Abcam gold antibody diluent. The dilute antibody (12 µl) was combined with 42 µl of the Abcam gold conjugation buffer in a 0.2 ml PCR tube (Axygen, Ref PCR-02-C). This solution (45 µl) was then combined with 50 µl of IJP solution in a PCR tube and mixed for 15 min at 1,000 rpm on a shaker. Abcam gold conjugation quencher was added (5 µl) to the solution, which reacted for either 15 min at room temperature or overnight at 4 °C. The functionalized IJPs were centrifuged in a Fisher AccuSpin Micro 17 at 6,000 × g for 5 min and washed with 1:400 Tween 20 (Sigma-Aldrich P9416-50ML) DI H₂O once, and twice with Dulbecco's PBS (catalogue number 02-0119-1000) 10 times diluted in DI H₂O, before being reconstituted in 50 µl of 10× diluted PBS. This IJP solution was combined with samples in a 2:1 ratio and allowed to incubate for an hour before imaging^{66,68}.

In this research, the antibodies utilized included CD63 mouse monoclonal antibody (Proteintech, catalogue number 67605-1-Ig, lot 10023876), CD81 rabbit polyclonal antibody (Proteintech, catalogue number 27855-1-AP, lot 00107630), glypican 1 rabbit polyclonal antibody (Proteintech, catalogue number 16700-1-AP, lot 00056068), CEA rabbit polyclonal antibody (Proteintech, catalogue number 10421-1-AP, lot 00017390), mouse IgG1 isotype control mouse monoclonal antibody (Proteintech, catalogue number 66360-1-Ig, lot 10028151) and Phospho-Tau181 monoclonal antibody (Invitrogen, reference MN1050, lots XF3582141 and YI4023267). Mab806 antibody (ABT-806, catalogue number TAB-228CL) was purchased from Creative Biolabs^{66,68}.

Fluorescence imaging of IJPs

After incubating with the sample, a 2 µl drop of the IJP solution was pipetted onto a standard glass microscope slide (VWR, catalogue number 48300-026). Three cover micro covers (VWR, catalogue number 48366-089) are stacked on either side of the drop to create a vertical spacing of 440 µm. Another cover slip was placed on top of the solution so that contact with the drop was made. The entire set-up was then placed on an Olympus IX-71 inverted fluorescence microscope above a 10× objective. An Olympus Optical 100 W High Pressure Mercury Burner (model number BH2-RFL-T3, number 2308002) was used to create the fluorescence in the experiments. The focal plane was set to ~220 µm above the slide during recording. Videos ranging from 60 s to 180 s were captured using a Retiga EXi (QImaging, catalogue number 01-RET-EXI-L-M-14-C) camera and a Basler ace 2 R (Basler, catalogue number a2A1920-160ucPRO) camera at a frame rate of 10 Hz. All trials were conducted with a minimum of three technical replicates^{66,68}.

Cell media preparation

DiFi cells, derived from human colorectal carcinoma, were cultured in a three-dimensional (3D) system to replicate the *in vivo* tumour microenvironment closely. The 3D scaffolds, constructed from type-I collagen at a concentration of 2 mg ml⁻¹, were layered in a tripartite structure: basal and top layers of pure collagen flanked a central layer embedding DiFi cells at a density of 5,000 cells per ml. This configuration was incubated at 37 °C in a humidified atmosphere of 5% CO₂. Culture medium was supplemented with 10% fetal bovine serum (FBS), 2 µg ml⁻¹ normocin, insulin–transferrin–selenium, epidermal growth factor, hydrocortisone and T3 thyroid hormone, and refreshed every 2–3 days^{66–68}.

The human melanoma cell line A375P (RRID CVCL_6233) and the human breast cancer cell line MDA-MB-468 (RRID CVCL_0419) were maintained in high-glucose Dulbecco's modified Eagle medium (DMEM, Gibco) enriched with 10% (v/v) EquaFetal Serum (Atlas Biologicals), 2 mM L-glutamine, 100 U ml⁻¹ penicillin–streptomycin and 1 mM sodium pyruvate. These cells were cultured under standard conditions at 37 °C in a 5% CO₂ humidified atmosphere, ensuring optimal growth and maintenance^{66–68}.

Mouse fibroblast cells (3T3) were cultured in minimum essential medium (MEM) supplemented with 10% FBS and 1% antibiotic–antimycotic solution. The cells were housed at 37 °C in a humidified 5% CO₂ environment. Passaging involved washing with 1× PBS, trypsinization with trypsin-EDTA and a recovery period of at least 1 day before experimental use. GBM9 glioblastoma cells were cultured as neurospheres in Neurobasal medium devoid of serum (Gibco) and supplemented with 3 mM GlutaMAX, 1× B-27 supplement, 0.5× N-2 supplement, 20 ng ml⁻¹ EGF (R&D Systems), 20 ng ml⁻¹ FGF (PEPROTECH) and 1% antibiotic–antimycotic solution (Corning). Passaging was performed using the NeuroCult Chemical Dissociation Kit-Mouse (Stemcell Technologies) following the manufacturer's guidelines^{66–68}. Although some other cell lines were also used, the isolated EVs/cell media from them were directly provided to the authors.

IJP immunostaining control

A quantum dot (Qdot) functionalization kit with an excitation/emission of 405/525 was first purchased from Thermo Fisher (catalogue number S10449). The Qdots underwent conjugation according to the manufacturer's protocol using a 100 µg cocktail of murine anti-human CD63 antibody (Proteintech, catalogue number 67605-1-Ig) and murine anti-human CD9 antibody (Proteintech, catalogue number 60232-1-Ig). IJPs functionalized with anti-CD63, as previously described, were mixed with purified sEVs of different concentrations for an hour and were then mixed with anti-CD63/anti-CD9 conjugated Qdot 525 for another hour. Then, the images were taken with a Leica Stellaris 8 DIVE confocal microscope using a 10× objective. Two preset filters, the red FluoSpheres filter and the Qdot525 filter, were used in the sequential

line scan mode to minimize spectral overlap and maximize fluorescent yield. All the images are unprocessed, and full images for each channel are available in the supplementary data^{66,68}.

UC

The isolation and quantification of sEVs from human plasma and concentrated cell media involve a detailed UC protocol. Initially, 200 μ l of human plasma is diluted with PBS to a final volume of 1 ml, or 1 ml of concentrated cell media is used directly (concentrated using 100 kDa filter from 10 ml to 1 ml). This mixture is centrifuged at $12,000 \times g$ for 20 min to remove larger particles. The supernatant is then passed through a 220 nm filter to eliminate larger debris. The filtered fluid is added on top of 3 ml of PBS in a 4 ml ultracentrifuge tube and ultracentrifuged at $167,000 \times g$ for 1.5 h using a swinging bucket rotor (Beckman Coulter SW60Ti), which is preferred for its efficiency in pelleting vesicles compared with fixed angle rotors. After UC, the supernatant is carefully removed, leaving about 0.2 ml to avoid disturbing the pellet, which is then resuspended in 0.5 ml of ice-cold PBS. For further purification, this resuspended solution is transferred on top of 15.5 ml of PBS in a 17 ml ultracentrifuge tube and ultracentrifuged at $167,000 \times g$ for 4.5 h (SW32.1Ti). This step aims to refine the sEVs by pelleting them again under high-speed centrifugation. After pelleting, the sEVs are resuspended and passed through a 300 kDa filter to remove soluble proteins, thus enhancing the purity of the sEV sample. This additional purification step ensures the isolation of high-quality sEVs, now ready for downstream analyses such as SPR to study their composition or concentration^{31,66,68}.

SPR-based characterization of isolated sEVs

Before experimentation, all instrument-specific pre-experimental protocols recommended by the SPR instrument manufacturer were followed, particularly those pertaining to ‘the maintenance chip’ section. The system was then allowed to operate for an additional 12 h using double-distilled water (DDI) in standby mode. Subsequent to this preparatory phase, the chip (Series S CM5 SPR chips, Cytiva, catalogue number 29149603) was docked and normalized using 70% glycerol, or as otherwise advised by the manufacturer. The running buffer was then switched to PBS and maintained for 2 h. Antibodies were buffer exchanged and resuspended in 10 mM MES buffer at a pH of 6.0. This solution was flowed over the SPR chip at a rate of $10 \mu\text{l min}^{-1}$, delivering $100 \mu\text{l}$ of 0.1 mg ml^{-1} antibodies for 2 min to ensure appropriate preconcentration behaviour. The selected flow channel was then prepared by flowing PBS until a stable baseline was achieved. To functionalize the channel, a coupling solution containing 20 mg each of EDC (1-ethyl-3-(3-dimethylaminopropyl)carbodiimide hydrochloride, Life Technologies, catalogue number 22980) and Sulfo-NHS (*N*-hydroxysulfosuccinimide, Life Technologies, catalogue number 24510) in 700 μl of 100 mM MES at pH 4.7 was flowed through the chip for 15 min at the same flow rate. Following this, approximately 400 μl of the antibody solution (0.1 mg ml^{-1} in 10 mM MES pH 6.0) was applied at $10 \mu\text{l min}^{-1}$ for 25 min. The reaction was quenched by flowing 0.1 M ethanolamine (Life Technologies, catalogue number 022793.30) for 2 min. The channel was then washed with PBS until a stable baseline was re-established. The extent of antibody functionalization was assessed by measuring the baseline shift before and after conjugation, with an expected increase of over 2,000 response units (RU) indicating successful antibody coupling^{31,66,68}.

Baseline establishment and experimental conditions for SPR measurements were conducted as follows: initially, the baseline was recorded to ensure stability, defined as a drift rate of less than 0.1 response units (RU) per minute. If the drift exceeded this threshold, the running buffer was flowed overnight or until the baseline stability criteria were met^{31,66,68}.

Upon achieving a stable baseline, experimental procedures commenced. Two flow rates, $1 \mu\text{l min}^{-1}$ and $10 \mu\text{l min}^{-1}$, were chosen

to cover a decade of flow rate variation while minimizing sample volume consumption. At the start of each cycle, the system was first set to a flow rate of $10 \mu\text{l min}^{-1}$: the running buffer was flowed for 5 min, followed by a sample injection in high-performance mode for 2 min. Subsequently, the system was washed with the running buffer for 60 s before sequentially injecting glycine-HCl (10 mM, pH 2) and 1% albumin, each for 20 s. The flow rate was then reduced to $1 \mu\text{l min}^{-1}$, and the running buffer was flowed for an additional 30 min, followed by a 5 min sample flow. The flow rate was subsequently restored to $10 \mu\text{l min}^{-1}$ for final wash steps and injection sequences identical to the initial set. For both flow rates, the slope of the sensor response between 30 s and 120 s post-injection was recorded to assess binding characteristics^{31,66,68}.

To correct for any system artefacts, a blank cycle was performed immediately following the sample measurements, using PBS instead of the sample to simulate identical injection conditions. The process was identical to that of the sample injections, including the adjustment of flow rates and the sequence of buffer and reagent injections. The measured slopes from the sample and blank cycles were compared to ascertain the specific binding response. These steps were repeated for each new sample, with the resultant signal representing the differential between the slopes obtained during sample and blank measurements, thus providing a corrected and reliable measure of the binding interactions. On the basis of the mass transfer constant in a laminar flow, size of sEVs, size of sensor chip and diffusivity of sEVs, they are converted to sEV number concentrations^{31,66,68}.

Data analysis assumptions and sample randomization

Data distribution was assumed to be normal, but this was not formally tested. To minimize bias, all samples were randomized before experimentation. Each sample was assigned a random number to ensure that the allocation process was unbiased and that experimental handling was consistent across groups. All IJP experiments conducted with clinical samples were performed under blinded conditions. Data collection and analysis were carried out without knowledge of sample identity. The data were only unblinded after all experimental measurements and data collection were completed, ensuring objectivity during the analysis phase.

Creating simulated plasma with varying non-sEV proportions at equivalent sEV concentrations

To produce simulated plasma, we first isolated the sEV and non-sEV matrix from 50-fold diluted plasma. This process yielded quantities of sEV and non-sEV matrix equivalent to those found in the original volume of diluted plasma. Specifically, we used V_1 ml of 50-fold diluted human plasma to generate V_2 ml of sEV and V_3 ml of the non-sEV matrix. To maintain a constant sEV concentration, we aimed to reproduce a specified percentage x (%) of the original non-sEV fraction while keeping the sEV fraction unchanged. We fix sEV concentration to the amount present in 1,000-fold diluted plasma, including for the 50-fold plasma, by diluting it 20 times^{66–68}.

For creating V_0 ml of a simulated sample that mimics the characteristics of 1,000-fold diluted plasma, we mixed the following components in specified proportions:

For 10% of the original non-sEV matrix fraction in proportion to sEV (1:0.1 sEV/non-sEV matrix in Fig. 2i)
 $= \frac{V_0 V_2}{20V_1}$ ml of isolated sEVs + $\frac{1}{10} \frac{V_0 V_3}{20V_1}$ ml of non-sEV matrix
+ $V_0 \left(1 - \frac{V_2}{20V_1} - \frac{1}{10} \frac{V_3}{20V_1}\right)$ of PBS.

For 1,000% of the original non-sEV matrix fraction in proportion to sEV (1:10 sEV/non-sEV matrix in Fig. 2i)
 $= \frac{V_0 V_2}{20V_1}$ ml of isolated sEVs + $\frac{V_0 V_3}{2V_1}$ ml of non-sEV matrix
+ $V_0 \left(1 - \frac{V_2}{20V_1} - \frac{V_3}{2V_1}\right)$ of PBS.

Reporting summary

Further information on research design is available in the Nature Portfolio Reporting Summary linked to this article.

Data availability

The source data are available in the Supplementary Information. Additional data can be obtained from the corresponding author upon request. Source data are provided with this paper.

Code availability

All primary codes critical to this study are provided in the supplementary data.

References

- Kalluri, R. & LeBleu, V. S. The biology, function, and biomedical applications of exosomes. *Science* **367**, eaau6977 (2020).
- Sabatke, B., Rossi, I. V., Sana, A., Bonato, L. B. & Ramirez, M. I. Extracellular vesicles biogenesis and uptake concepts: a comprehensive guide to studying host-pathogen communication. *Mol. Microbiol.* **122**, 613–629 (2023).
- Kottorou, A. et al. Small extracellular vesicles (sEVs) biogenesis molecular players are associated with clinical outcome of colorectal cancer patients. *Cancers* **15**, 1685 (2023).
- Li, J., Zhang, Y., Dong, P. Y., Yang, G. M. & Gurunathan, S. A comprehensive review on the composition, biogenesis, purification, and multifunctional role of exosome as delivery vehicles for cancer therapy. *Biomed. Pharmacother.* **165**, 115087 (2023).
- Cavallaro, S. et al. Label-free surface protein profiling of extracellular vesicles by an electrokinetic sensor. *ACS Sens.* **4**, 1399–1408 (2019).
- Mustapic, M. et al. Plasma extracellular vesicles enriched for neuronal origin: a potential window into brain pathologic processes. *Front. Neurosci.* **11**, 278 (2017).
- Gao, R. & Li, X. Extracellular vesicles and pathological cardiac hypertrophy. *Adv. Exp. Med. Biol.* **1418**, 17–31 (2023).
- Michel, L. Y. M. Extracellular vesicles in adipose tissue communication with the healthy and pathological heart. *Int. J. Mol. Sci.* **24**, 7745 (2023).
- Xiong, M. et al. Exosomes from adipose-derived stem cells: the emerging roles and applications in tissue regeneration of plastic and cosmetic surgery. *Front. Cell Dev. Biol.* **8**, 574223 (2020).
- Zheng, X., Bahr, M. & Doepfner, T. R. From tumor metastasis towards cerebral ischemia-extracellular vesicles as a general concept of intercellular communication processes. *Int. J. Mol. Sci.* **20**, 5995 (2019).
- Maacha, S. et al. Extracellular vesicles-mediated intercellular communication: roles in the tumor microenvironment and anti-cancer drug resistance. *Mol. Cancer* **18**, 55 (2019).
- Latifi, Z., Fattahi, A., Ranjbaran, A., Nejabati, H. R. & Imakawa, K. Potential roles of metalloproteinases of endometrium-derived exosomes in embryo-maternal crosstalk during implantation. *J. Cell. Physiol.* **233**, 4530–4545 (2018).
- Yu, W. et al. Exosome-based liquid biopsies in cancer: opportunities and challenges. *Ann. Oncol.* **32**, 466–477 (2021).
- Hakulinen, J., Sankkila, L., Sugiyama, N., Lehti, K. & Keski-Oja, J. Secretion of active membrane type 1 matrix metalloproteinase (MMP-14) into extracellular space in microvesicular exosomes. *J. Cell. Biochem.* **105**, 1211–1218 (2008).
- Silva, V. O. et al. Extracellular vesicles isolated from *Toxoplasma gondii* induce host immune response. *Parasite Immunol.* **40**, e12571 (2018).
- Brisson, A. R., Tan, S., Linares, R., Gounou, C. & Arraud, N. Extracellular vesicles from activated platelets: a semi-quantitative cryo-electron microscopy and immuno-gold labeling study. *Platelets* **28**, 263–271 (2017).
- Cocucci, E. & Meldolesi, J. Ectosomes and exosomes: shedding the confusion between extracellular vesicles. *Trends Cell Biol.* **25**, 364–372 (2015).
- Jackson, H. K. et al. Extracellular vesicles potentiate medulloblastoma metastasis in an EMMPRIN and MMP-2 dependent manner. *Cancers* **15**, 2601 (2023).
- Liguori, G. L. & Kralj-Iglic, V. Pathological and therapeutic significance of tumor-derived extracellular vesicles in cancer cell migration and metastasis. *Cancers* **15**, 4425 (2023).
- Li, A., Zhang, T., Zheng, M., Liu, Y. & Chen, Z. Exosomal proteins as potential markers of tumor diagnosis. *J. Hematol. Oncol.* **10**, 175 (2017).
- Chen, I. H. et al. Phosphoproteins in extracellular vesicles as candidate markers for breast cancer. *Proc. Natl Acad. Sci. USA* **114**, 3175–3180 (2017).
- Taller, D. et al. On-chip surface acoustic wave lysis and ion-exchange nanomembrane detection of exosomal RNA for pancreatic cancer study and diagnosis. *Lab Chip* **15**, 1656–1666 (2015).
- Melo, S. A. et al. Glypican-1 identifies cancer exosomes and detects early pancreatic cancer. *Nature* **523**, 177–182 (2015).
- Bryja, A. et al. Small extracellular vesicles—a host for advanced bioengineering and ‘Trojan Horse’ of non-coding RNAs. *Life Sci.* **332**, 122126 (2023).
- Patras, L. & Banciu, M. Intercellular crosstalk via extracellular vesicles in tumor milieu as emerging therapies for cancer progression. *Curr. Pharm. Des.* **25**, 1980–2006 (2019).
- Vandergriff, A. et al. Targeting regenerative exosomes to myocardial infarction using cardiac homing peptide. *Theranostics* **8**, 1869–1878 (2018).
- Antes, T. J. et al. Targeting extracellular vesicles to injured tissue using membrane cloaking and surface display. *J. Nanobiotechnol.* **16**, 61 (2018).
- Gilligan, K. E. & Dwyer, R. M. Engineering exosomes for cancer therapy. *Int. J. Mol. Sci.* **18**, 1122 (2017).
- Zhang, Q. et al. Supermeres are functional extracellular nanoparticles replete with disease biomarkers and therapeutic targets. *Nat. Cell Biol.* **23**, 1240–1254 (2021).
- Jeppesen, D. K. et al. Reassessment of exosome composition. *Cell* **177**, 428–445.e418 (2019).
- Maniya, N. H. et al. An anion exchange membrane sensor detects EGFR and its activity state in plasma CD63 extracellular vesicles from patients with glioblastoma. *Commun. Biol.* **7**, 677 (2024).
- Kumar, S., Maniya, N., Wang, C., Senapati, S. & Chang, H. C. Quantifying PON1 on HDL with nanoparticle-gated electrokinetic membrane sensor for accurate cardiovascular risk assessment. *Nat. Commun.* **14**, 557 (2023).
- Grey, M. et al. Acceleration of alpha-synuclein aggregation by exosomes. *J. Biol. Chem.* **290**, 2969–2982 (2015).
- Guo, M. et al. Microglial exosomes facilitate alpha-synuclein transmission in Parkinson's disease. *Brain* **143**, 1476–1497 (2020).
- Yu, P. et al. The incorporation of acetylated LAP-TGF-beta1 proteins into exosomes promotes TNBC cell dissemination in lung micro-metastasis. *Mol. Cancer* **23**, 82 (2024).
- Kumar, S., Senapati, S. & Chang, H. C. Extracellular vesicle and lipoprotein diagnostics (ExoLP-Dx) with membrane sensor: a robust microfluidic platform to overcome heterogeneity. *Biomicrofluidics* **18**, 041301 (2024).
- Zhai, C. et al. Precise identification and profiling of surface proteins of ultra rare tumor specific extracellular vesicle with dynamic quantitative plasmonic imaging. *ACS Nano* **17**, 16656–16667 (2023).
- Li, Z. et al. Surface-modified mesoporous nanofibers for microfluidic immunosensor with an ultra-sensitivity and high signal-to-noise ratio. *Biosens. Bioelectron.* **166**, 112444 (2020).

39. Zhang, Q., Jeppesen, D. K., Higginbotham, J. N., Franklin, J. L. & Coffey, R. J. Comprehensive isolation of extracellular vesicles and nanoparticles. *Nat. Protoc.* **18**, 1462–1487 (2023).
40. Jeyaram, A. & Jay, S. M. Preservation and storage stability of extracellular vesicles for therapeutic applications. *AAPS J.* **20**, 1 (2017).
41. Sodar, B. W. et al. Low-density lipoprotein mimics blood plasma-derived exosomes and microvesicles during isolation and detection. *Sci. Rep.* **6**, 24316 (2016).
42. Li, C. et al. Cerebrospinal fluid-derived extracellular vesicles after spinal cord injury promote vascular regeneration via PI3K/AKT signaling pathway. *J. Orthop. Transl.* **39**, 124–134 (2023).
43. Hagey, D. W. et al. Extracellular vesicles are the primary source of blood-borne tumour-derived mutant KRAS DNA early in pancreatic cancer. *J. Extracell. Vesicles* **10**, e12142 (2021).
44. Kharmate, G., Hosseini-Beheshti, E., Caradec, J., Chin, M. Y. & Tomlinson Guns, E. S. Epidermal growth factor receptor in prostate cancer derived exosomes. *PLoS ONE* **11**, e0154967 (2016).
45. Beckham, C. J. et al. Bladder cancer exosomes contain EDIL-3/Del1 and facilitate cancer progression. *J. Urol.* **192**, 583–592 (2014).
46. Coumans, F. A. W. et al. Methodological guidelines to study extracellular vesicles. *Circ. Res.* **120**, 1632–1648 (2017).
47. Lotvall, J. et al. Minimal experimental requirements for definition of extracellular vesicles and their functions: a position statement from the International Society for Extracellular Vesicles. *J. Extracell. Vesicles* **3**, 26913 (2014).
48. Witwer, K. W. et al. Updating the MISEV minimal requirements for extracellular vesicle studies: building bridges to reproducibility. *J. Extracell. Vesicles* **6**, 1396823 (2017).
49. Witwer, K. W. et al. Updating MISEV: evolving the minimal requirements for studies of extracellular vesicles. *J. Extracell. Vesicles* **10**, e12182 (2021).
50. Welsh, J. A. et al. Minimal information for studies of extracellular vesicles (MISEV2023): from basic to advanced approaches. *J. Extracell. Vesicles* **13**, e12404 (2024).
51. Costa, V. F. A. et al. Platelet-derived microvesicles contribute to the pathophysiology of human cutaneous leishmaniasis: a nano-flow cytometric approach in plasma samples from patients before and under antimonial treatment. *Microorganisms* **12**, 526 (2024).
52. Lees, R. et al. Single extracellular vesicle transmembrane protein characterization by nano-flow cytometry. *J. Vis. Exp.* **185**, e64020 (2022).
53. Chen, C. et al. Quantitative assessment of lipophilic membrane dye-based labelling of extracellular vesicles by nano-flow cytometry. *J. Extracell. Vesicles* **12**, e12351 (2023).
54. Li, L. et al. Development of spectral nano-flow cytometry for high-throughput multiparameter analysis of individual biological nanoparticles. *Anal. Chem.* **95**, 3423–3433 (2023).
55. Breitwieser, K. et al. Detailed characterization of small extracellular vesicles from different cell types based on tetraspanin composition by ExoView R100 platform. *Int. J. Mol. Sci.* **23**, 8544 (2022).
56. Price, J. M. J. et al. Detection of tissue factor-positive extracellular vesicles using the ExoView R100 system. *Res. Pract. Thromb. Haemost.* **7**, 100177 (2023).
57. Fortunato, D. et al. Opportunities and pitfalls of fluorescent labeling methodologies for extracellular vesicle profiling on high-resolution single-particle platforms. *Int. J. Mol. Sci.* **22**, 10510 (2021).
58. Huang, G. et al. Single small extracellular vesicle (sEV) quantification by upconversion nanoparticles. *Nano Lett.* **22**, 3761–3769 (2022).
59. Atherton, T. J. & Kerbyson, D. J. Size invariant circle detection. *Image Vis. Comput.* **17**, 795–803 (1999).
60. Yuen, H., Princen, J., Illingworth, J. & Kittler, J. Comparative study of Hough transform methods for circle finding. *Image Vis. Comput.* **8**, 71–77 (1990).
61. Davies, E. R. *Machine Vision: Theory, Algorithms, Practicalities* (Elsevier, 2004).
62. Norman, M. et al. L1CAM is not associated with extracellular vesicles in human cerebrospinal fluid or plasma. *Nat. Methods* **18**, 631–634 (2021).
63. Jung, H., Robison, A. D. & Cremer, P. S. Detecting protein-ligand binding on supported bilayers by local pH modulation. *J. Am. Chem. Soc.* **131**, 1006–1014 (2009).
64. Su, P. et al. SI-traceable calibration-free analysis for the active concentration of G2-EPSPS protein using surface plasmon resonance. *Talanta* **178**, 78–84 (2018).
65. Visentin, J., Minder, L., Lee, J. H., Taupin, J. L. & Di Primo, C. Calibration free concentration analysis by surface plasmon resonance in a capture mode. *Talanta* **148**, 478–485 (2016).
66. Kumar, S. et al. Immunojanus particles for low-volume and isolation-free unlabeled characterization of small extracellular vesicle in biofluids: characterization of disease type by surface marker profiling. Preprint at *bioRxiv* (2025).
67. Kumar, S. et al. Surface markers on supermeres outperform extracellular vesicles in colorectal cancer diagnosis. *Sci. Rep.* **16**, 5989 (2026).
68. Shi, T. H. et al. Multimodal activity-affinity assay of ADAM-10 extracellular vesicles in untreated plasma reveals metastatic stage of colorectal cancer. *Biosens. Bioelectron.* **302**, 118517 (2026).
69. Landry, J. P., Ke, Y., Yu, G. L. & Zhu, X. D. Measuring affinity constants of 1450 monoclonal antibodies to peptide targets with a microarray-based label-free assay platform. *J. Immunol. Methods* **417**, 86–96 (2015).

Acknowledgements

This work was partially supported by the NIH Commons Fund, through the Office of Strategic Coordination/Office of NIH Director, 1UH3CA241684-01 (H.-C.C. and S.S.). We are also grateful for cell media samples from R. Coffey, A. Charest, Y. Wang and C. D'Souza-Schorey. We would like to acknowledge Notre Dame Integrated Imaging Facility (NDIIF) at Notre Dame. We would also like to thank the Notre Dame Biophysics Instrumentation Core Facility for use of the Biacore T200 SPR system, purchased with funding from NIH (S10 ODO28553). S.K. would like to acknowledge O'Brien Fellowship from Berthiaume Institute of Precision Health (BIPH) at Notre Dame. This project was made possible, in part, with support from the Indiana Biobank and the Indiana Clinical and Translational Sciences Institute funded, in part, by grant number UM1T004402 and the Lilly Endowment.

Author contributions

H.-C.C. and H.-S.C. conceived the project. S.K. and J.A.S. designed the experiments, ran the IJP experiments, analysed the experimental results and completed the data processing. S.K. and J.A.S. also did the UC+SPR and made all the figures for this paper. S.S. and J.A.S. optimized the functionalization of IJPs. S.K. and J.A.S. optimized the entire IJP workflow. T.S., S.K. and J.A.S. performed the NTA. S.K. and H.-C.C. optimized the code for automated IJP blinking detection. All authors contributed to writing the paper.

Competing interests

The authors declare no competing interests.

Additional information

Supplementary information The online version contains supplementary material available at <https://doi.org/10.1038/s41551-026-01632-8>.

Correspondence and requests for materials should be addressed to Hsueh-Chia Chang.

Peer review information *Nature Biomedical Engineering* thanks the anonymous reviewers for their contribution to the peer review of this work. Peer reviewer reports are available.

Reprints and permissions information is available at www.nature.com/reprints.

Publisher's note Springer Nature remains neutral with regard to jurisdictional claims in published maps and institutional affiliations.

Springer Nature or its licensor (e.g. a society or other partner) holds exclusive rights to this article under a publishing agreement with the author(s) or other rightsholder(s); author self-archiving of the accepted manuscript version of this article is solely governed by the terms of such publishing agreement and applicable law.

© The Author(s), under exclusive licence to Springer Nature Limited 2026

Reporting Summary

Nature Portfolio wishes to improve the reproducibility of the work that we publish. This form provides structure for consistency and transparency in reporting. For further information on Nature Portfolio policies, see our [Editorial Policies](#) and the [Editorial Policy Checklist](#).

Statistics

For all statistical analyses, confirm that the following items are present in the figure legend, table legend, main text, or Methods section.

n/a Confirmed

- The exact sample size (n) for each experimental group/condition, given as a discrete number and unit of measurement
- A statement on whether measurements were taken from distinct samples or whether the same sample was measured repeatedly
- The statistical test(s) used AND whether they are one- or two-sided
Only common tests should be described solely by name; describe more complex techniques in the Methods section.
- A description of all covariates tested
- A description of any assumptions or corrections, such as tests of normality and adjustment for multiple comparisons
- A full description of the statistical parameters including central tendency (e.g. means) or other basic estimates (e.g. regression coefficient) AND variation (e.g. standard deviation) or associated estimates of uncertainty (e.g. confidence intervals)
- For null hypothesis testing, the test statistic (e.g. F , t , r) with confidence intervals, effect sizes, degrees of freedom and P value noted
Give P values as exact values whenever suitable.
- For Bayesian analysis, information on the choice of priors and Markov chain Monte Carlo settings
- For hierarchical and complex designs, identification of the appropriate level for tests and full reporting of outcomes
- Estimates of effect sizes (e.g. Cohen's d , Pearson's r), indicating how they were calculated

Our web collection on [statistics for biologists](#) contains articles on many of the points above.

Software and code

Policy information about [availability of computer code](#)

Data collection

Data analysis

For manuscripts utilizing custom algorithms or software that are central to the research but not yet described in published literature, software must be made available to editors and reviewers. We strongly encourage code deposition in a community repository (e.g. GitHub). See the Nature Portfolio [guidelines for submitting code & software](#) for further information.

Data

Policy information about [availability of data](#)

All manuscripts must include a [data availability statement](#). This statement should provide the following information, where applicable:

- Accession codes, unique identifiers, or web links for publicly available datasets
- A description of any restrictions on data availability
- For clinical datasets or third party data, please ensure that the statement adheres to our [policy](#)

Research involving human participants, their data, or biological material

Policy information about studies with [human participants or human data](#). See also policy information about [sex, gender \(identity/presentation\), and sexual orientation](#) and [race, ethnicity and racism](#).

Reporting on sex and gender	The sample size is not large enough to do any gender or sex based analysis
Reporting on race, ethnicity, or other socially relevant groupings	No such categorization was done.
Population characteristics	N/A
Recruitment	Samples were received from commercial sources like Precision for Medicine and a health institute ONJCRI, Melbourne, Australia that have their own protocol for recruitment.
Ethics oversight	University of Notre Dame

Note that full information on the approval of the study protocol must also be provided in the manuscript.

Field-specific reporting

Please select the one below that is the best fit for your research. If you are not sure, read the appropriate sections before making your selection.

Life sciences Behavioural & social sciences Ecological, evolutionary & environmental sciences

For a reference copy of the document with all sections, see [nature.com/documents/nr-reporting-summary-flat.pdf](https://www.nature.com/documents/nr-reporting-summary-flat.pdf)

Life sciences study design

All studies must disclose on these points even when the disclosure is negative.

Sample size	This study was a pilot study designed to explore the feasibility and preliminary outcomes of the investigated variables. As is standard practice for pilot studies, a formal sample size calculation was not conducted. The primary aim was to gather initial data and insights to inform the design and power calculation of future, larger-scale studies.
Data exclusions	None of data was excluded.
Replication	Each IJP experiment was averaged over at least three technical replicates.
Randomization	No randomization was done for the calibration curves. Patient samples were de-labeled and randomized for all IJP experiments.
Blinding	The person performing the experiments were blinded to all the clinical samples with results revealed in the end.

Reporting for specific materials, systems and methods

We require information from authors about some types of materials, experimental systems and methods used in many studies. Here, indicate whether each material, system or method listed is relevant to your study. If you are not sure if a list item applies to your research, read the appropriate section before selecting a response.

Materials & experimental systems

n/a	Involvement in the study
<input type="checkbox"/>	<input checked="" type="checkbox"/> Antibodies
<input type="checkbox"/>	<input checked="" type="checkbox"/> Eukaryotic cell lines
<input checked="" type="checkbox"/>	<input type="checkbox"/> Palaeontology and archaeology
<input checked="" type="checkbox"/>	<input type="checkbox"/> Animals and other organisms
<input type="checkbox"/>	<input checked="" type="checkbox"/> Clinical data
<input checked="" type="checkbox"/>	<input type="checkbox"/> Dual use research of concern
<input checked="" type="checkbox"/>	<input type="checkbox"/> Plants

Methods

n/a	Involvement in the study
<input checked="" type="checkbox"/>	<input type="checkbox"/> ChIP-seq
<input checked="" type="checkbox"/>	<input type="checkbox"/> Flow cytometry
<input checked="" type="checkbox"/>	<input type="checkbox"/> MRI-based neuroimaging

Antibodies

Antibodies used	Antibody Name Catalogue no. Lot number
-----------------	--

From ProteinTech:
 CD63 Mouse McAb : 67605-1-Ig : 10023876 (x4)
 CD9 Mouse McAb : 60232-1-Ig : 10021366
 CD81 Rabbit PolyAb : 27855-1-AP : 00107630
 Glypican 1 Rabbit PolyAb : 16700-1-AP : 00056068 (x2)
 CEA Rabbit PolyAb : 10421-1-AP : 00017390 (x4)
 Mouse IgG1 isotype control Mouse McAb : 66360-1-Ig : 10028151

From Invitrogen:
 Phospho-Tau181 mono : Ref MN1050 : XF3582141 (x1), YI4023267 (x1)

Validation

Done by the manufacturer. No additional verification done by the authors.
www.ptglab.com
www.thermofisher.com/us/en/home.html

Eukaryotic cell lines

Policy information about [cell lines and Sex and Gender in Research](#)

Cell line source(s)

DiFi – Human colorectal adenocarcinoma cell line. Commercially obtained (ATCC)
 GBM6 – Patient-derived glioblastoma multiforme line obtained from Prof Al Charest, Harvard
 MDA-MB-468 – Human triple-negative breast cancer cell line (ATCC)
 A375P – Human melanoma cell line (A375 parental), (ATCC)
 3T3 – Mouse embryonic fibroblast cell line (ATCC)

Authentication

All cell lines were authenticated by the original vendors using STR profiling. No additional authentication was performed by the authors.

Mycoplasma contamination

Cell lines were not tested for mycoplasma contamination by the authors

Commonly misidentified lines
(See [ICLAC](#) register)

None of the cell lines used (DiFi, GBM6, MDA-MB-468, A375P, 3T3) are listed by ICLAC as commonly misidentified. These lines are widely used and well-characterized in the literature.

Clinical data

Policy information about [clinical studies](#)

All manuscripts should comply with the ICMJE [guidelines for publication of clinical research](#) and a completed [CONSORT checklist](#) must be included with all submissions.

Clinical trial registration

N/A

Study protocol

N/A

Data collection

N/A

Outcomes

N/A

Plants

Seed stocks

N/A

Novel plant genotypes

N/A

Authentication

N/A